Journal of Materials Chemistry A

Solar Hydrogen Production via Z-Scheme Water Splitting System Based Solely on Perovskite-type Tantalum Oxynitrides

Journal:	*Journal of Materials Chemistry A*
Manuscript ID	TA-ART-10-2024-007592.R1
Article Type:	Paper
Date Submitted by the Author:	06-Dec-2024

Complete List of Authors:	Li, Wenpeng; Shinshu University Faculty of Engineering, Graduate School of Medicine, Science and Technology Hirako, Akio; Shinshu University Faculty of Engineering, Graduate School of Science and Technology Sekimori, Shuji; Shinshu University Faculty of Engineering, Graduate School of Science and Technology Galvão, Rhauane; Shinshu Daigaku Nakabayashi, Mamiko; The University of Tokyo, Institute of Engineering Innovation, School of Engineering, Wang, Faze; Shinshu University Faculty of Engineering, Research Initiative for Supra-Materials Hisatomi, Takashi; Shinshu University, Institute for Aqua Regeneration Domen, Kazunari; The University of Tokyo, Office of University Professors; Shinshu University Interdisciplinary Cluster for Cutting Edge Research, Research Initiative for Supra-Materials; Kyung Hee University Department of Chemistry

ARTICLE

Solar Hydrogen Production via Z-Scheme Water Splitting System Based Solely on Perovskite-type Tantalum Oxynitrides

Wenpeng Li,[a] Akio Hirako,[b] Shuji Sekimori,[b] Rhauane Almeida Galvão,[a] Mamiko Nakabayashi,[c] Faze Wang,[d] Takashi Hisatomi,[*e] Kazunari Domen [*e,f,g]

Received 00th January 20xx,
Accepted 00th January 20xx

DOI: 10.1039/x0xx00000x

Z-scheme overall water splitting (ZOWS) systems can provide efficient hydrogen production in response to visible light. However, the integration of narrow-bandgap non-oxide photocatalysts as oxygen evolution photocatalysts (OEPs) in such systems remains underexplored. This lack of research arises because existing OEPs and the associated cocatalysts are typically employed to promote oxygen evolution in aqueous silver nitrate solutions and are less effective in ZOWS systems utilizing reversible redox mediators that are prone to backward reactions. The present work synthesized particulate single-crystalline $SrTaO_2N$ with exposed {100} and {110} facets using NaCl as a molten salt. The strategic use of Pt and CoO_x as dual cocatalysts to promote reduction and oxidation reactions, respectively, significantly enhanced the reduction of $[Co(bpy)_3]^{3+}$ ions and improved charge carrier separation. The resulting ZOWS system, employing $Pt/CoO_x/SrTaO_2N$ as the OEP, $Cr_2O_3/Pt/BaTaO_2N$ as the hydrogen evolution photocatalyst and $[Co(bpy)_3]^{3+/2+}$ as the redox mediator, achieved stoichiometric H_2 and O_2 evolution. This oxynitride-based system extends the visible light range available for ZOWS to nearly 600 nm, providing a new platform for solar hydrogen production. This work provides important insights into the application of narrow-bandgap oxynitride photocatalysts in ZOWS systems.

Introduction

Z-scheme overall water splitting (ZOWS), which allows the use of long-wavelength visible light in conjunction with narrow-bandgap photocatalysts, represents a viable strategy for photocatalytic H_2 production based on solar energy.[1-6] Various materials, including oxides, (oxy)sulfides, (oxy)nitrides, conjugated polymers and metal-organic frameworks, have been utilized as hydrogen evolution photocatalysts (HEPs) in ZOWS systems.[7-14] Among these, perovskite-type tantalum oxynitrides having the general formula $ATa(O,N)_3$ (with A representing Ca, Sr, Ba or La) have attracted attention. These compounds exhibit narrow bandgaps of 1.9 to 2.4 eV along with superior photochemical stability and optimal band-edge positions suitable for water splitting.[8, 15, 16] In particular, $BaTaO_2N$, with an absorption-edge wavelength of 650 nm, has been widely used as an HEP for ZOWS systems.[17-20] However, in present-day ZOWS systems employing $BaTaO_2N$, the absorption edges of the oxygen evolution photocatalysts (OEPs), including WO_3 and $BiVO_4$, are typically below 520 nm, such that a significant portion of the visible light spectrum is not used.[17, 21, 22] For this reason, it would be beneficial to develop OEPs with longer absorption edges so as to fully utilize solar radiation and achieve sufficient solar-to-hydrogen energy conversion efficiencies.

$SrTaO_2N$, another perovskite-type tantalum-based oxynitride having an absorption edge closer to 600 nm, shows promise as an OEP.[8, 23, 24] Various strategies, including cation doping, solid solution engineering, surface modification and cocatalyst modification, have been employed to increase the apparent quantum yield (AQY) associated with the O_2 evolution reaction to above 10% at 420 nm.[25, 26] However, the use of $SrTaO_2N$ as an OEP in Z-scheme systems has rarely been reported. Work to date involving OEPs and various cocatalysts has typically examined reactions involving O_2 evolution from aqueous silver nitrate solutions. Such systems are not well-suited to the study of ZOWS, which normally involves reversible redox mediators prone to backward reactions.

Photocatalyst crystal facet engineering has the potential to enhance photocatalytic performance by exploiting charge separation resulting from anisotropy. Research to date has examined water splitting by materials such as TiO_2, $SrTiO_3$ and $BiVO_4$.[17, 27-30] Recently, photocatalytic overall water splitting with an AQY of up to 96% (equivalent to an internal quantum yield of unity), was achieved under near ultraviolet radiation (350-360 nm). This was accomplished via the selective deposition of Cr_2O_3/Rh and CoOOH on different facets of Al-

[a] Graduate School of Medicine, Science and Technology, Shinshu University, Nagano, Japan.
[b] Graduate School of Science and Technology, Shinshu University, Nagano, Japan.
[c] Institute of Engineering Innovation, School of Engineering, The University of Tokyo, Tokyo, Japan.
[d] Research Initiative for Supra-Materials, Shinshu University, Nagano, Japan
[e] Institute for Aqua Regeneration, Shinshu University, Nagano, Japan
hisatomi@shinshu-u.ac.jp, domen@shinshu-u.ac.jp
[f] Office of University Professors, The University of Tokyo, Tokyo, Japan
[g] Department of Chemistry, Kyung Hee University, Republic of Korea
* Corresponding authors.
Supplementary Information available: [details of any supplementary information available should be included here]. See DOI: 10.1039/x0xx00000x

doped $SrTiO_3$ where these materials served as HER and OER cocatalysts, respectively. In such cases, the electric field resulting from work function differences facilitates the spatial separation of photogenerated electrons and holes, enabling targeted cocatalyst deposition. This spatial separation also enhances charge separation and surface catalysis while suppressing charge recombination and the unwanted O_2 reduction reaction, resulting in superior photocatalytic performance.[27] Therefore, it would be desirable to develop methods to synthesize $SrTaO_2N$ having controlled crystal facets. The coloading of dual cocatalysts on the surface of this type of photocatalyst represents a promising strategy for optimizing $SrTaO_2N$ as an OEP in ZOWS systems.

In the present study, a ZOWS system based exclusively on oxynitrides and capable of harnessing visible light up to 600 nm or longer was designed and evaluated. This system employed $Pt/CoO_x/SrTaO_2N$ as the OEP, $Cr_2O_3/Pt/BaTaO_2N$ as the HEP and $[Co(bpy)_3]^{3+/2+}$ as the redox mediator. The sequential loading of Pt and CoO_x as cocatalysts to promote reduction and oxidation reactions, respectively, enhanced charge-carrier separation and $[Co(bpy)_3]^{3+}$ reduction. In this manner, the water splitting efficiency was optimized.

Results and Discussion

The molten-salt method, also known as the flux method, offers a straightforward, cost-effective approach to crystal growth, allowing for the tuning of morphology, crystallinity and crystal size.[8, 31-34] In this work, powdered Ta_2O_5, $SrCO_3$ and NaCl were combined in a Ta:Sr:Na molar ratio of 1:1.1:9 and then subjected to nitridation under a flow of gaseous NH_3 at 1223 K for 6 h to obtain $SrTaO_2N$ as an orange powder. Analysis using X-ray diffraction (XRD) (Figure 1a) showed that this product comprised a $SrTaO_2N$ phase with a characteristic cubic perovskite structure (Fm3m).[8,2525, 32] UV-visible diffuse-reflectance spectroscopy (DRS) data (Figure 1b) demonstrated that this material had an absorption edge at 590 nm. The $SrTaO_2N$ nanocrystals exhibited very weak background absorption at longer wavelengths (>600 nm), indicating a low defect density.[32] Interestingly, this $SrTaO_2N$ synthesized via the molten-salt method was also found to possess a regular cubic morphology with particles of up to 500 nm in size and distinct crystal facets (Figure 1c) associated with the {100} and {110} planes. The formation of these different exposed crystal facets is attributed to interactions that occurred during the crystal growth process. Specifically, Na^+ ions from the molten salt were adsorbed on the rapidly growing surfaces and subsequently altered the electrostatic interactions between the $SrTaO_2N$ particles. This modification impeded growth along the more stable {100} planes, thereby promoting the formation of {110} planes.[25, 35] As shown in Figure 1d, Pt nanoparticles were preferentially loaded onto the {100} facets during reductive photodeposition, indicating that photogenerated electrons reacted predominantly on these facets. This phenomenon occurred because the difference in work functions between the {110} and {100} facets of the $SrTaO_2N$ generated a built-in electric field, as has been observed for various oxides and oxynitrides.[17, 27-29, 35] This field, in turn, drove the spatial separation of photogenerated charge carriers, directing electrons to the {100} facets and holes to the {110} facets (Figure 1e). In this process, the addition of molten NaCl was essential for the formation of $SrTaO_2N$ single crystals with well-defined facets.[32] In other trials, the direct nitridation of a mixture of Ta_2O_5 and $SrCO_3$ having a molar ratio of 0.5:1.1 was performed under identical conditions using the solid-state reaction (SSR) method without NaCl. The product, denoted herein as $SrTaO_2N$(SSR), contained Sr_3TaO_5 as an impurity phase (see Figure S1a in the Electronic Supplementary Information (ESI)). The increased full width at half-maximum of the characteristic XRD peaks related to the $SrTaO_2N$ phase indicated that the $SrTaO_2N$(SSR) had a low degree of crystallinity. Scanning electron microscopy (SEM) images also showed an irregular morphology, suggesting incomplete nitridation (Figure S1b).

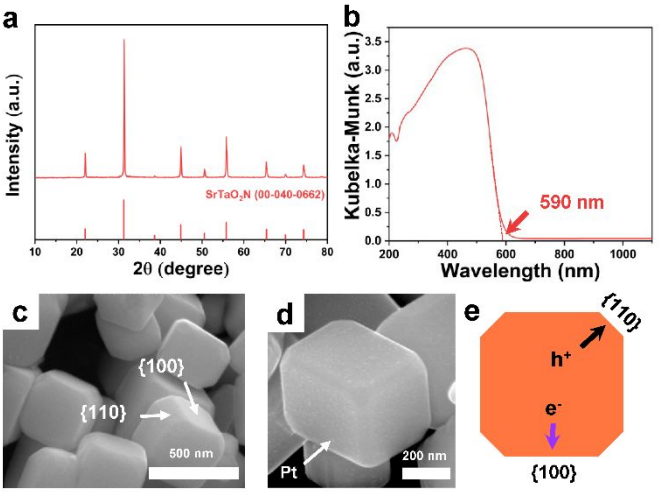

Figure 1. (a) XRD pattern, (b) UV-visible DRS spectrum, and (c) SEM image for $SrTaO_2N$ sample. (d) SEM image of $SrTaO_2N$ loaded with 1 wt% Pt by photodeposition. (e) Diagram showing migration of photogenerated electrons and holes in $SrTaO_2N$ particle with exposed {100} and {110} crystal facets.

The applicability of $SrTaO_2N$ as an OEP in a ZOWS system was assessed using $[Co(bpy)_3]^{3+/2+}$ as the redox mediator pair and $Cr_2O_3/Pt/BaTaO_2N$:Zr as the HEP. The $[Co(bpy)_3]^{3+/2+}$ pair was chosen due to the mild reaction conditions and excellent stability of this mediator.[26, 36] The $BaTaO_2N$:Zr was synthesized using a molten salt-assisted one-step nitridation process and subsequently loaded with a Cr_2O_3-coated Pt cocatalyst according to previously reported procedures (Figures S2 and S3).[20]

Figure 2a summarizes the effect of the method used to load the Pt cocatalyst onto the $SrTaO_2N$ on the ZOWS performance. In the case of the ZOWS system employing $SrTaO_2N$ with CoO_x as the sole cocatalyst, only H_2 was evolved. This result is ascribed to the inability of the photogenerated electrons in the $SrTaO_2N$ to reduce the $[Co(bpy)_3]^{3+}$. In contrast, loading the $CoO_x/SrTaO_2N$ with Pt by photodeposition (labelled in the figure as Pt(PD)) resulted in the ongoing simultaneous evolution of H_2 and O_2 in an almost stoichiometric ratio. The Pt

cocatalyst was evidently capable of both capturing and utilizing photogenerated electrons for the reduction of the $[Co(bpy)_3]^{3+}$ ions, thus increasing the extent of charge separation and promoting the ZOWS activity. It should also be noted that the method used to deposit the Pt cocatalyst had an important effect. Specifically, $CoO_x/SrTaO_2N$ loaded with Pt by impregnation (Pt(IMP)) exhibited less activity with almost no O_2 evolution. This change can be ascribed to the non-site selective deposition of Pt, which inhibited charge separation and lowered the usefulness of CoO_x particles as O_2 evolution sites. The system employing the $SrTaO_2N$(SSR) modified with the same cocatalysts (CoO_x and Pt(PD)) as the OEP failed to achieve overall water splitting. These observations underscore the crucial role of high crystallinity and anisotropic crystal facets in enhancing photocatalytic performance. These data also highlight the superiority of the molten-salt flux method in terms of producing highly crystalline $SrTaO_2N$ single crystals having specific exposed facets.

After optimizing the loading of the dual CoO_x and Pt(PD) cocatalysts (Figure S5), this system simultaneously evolved H_2 and O_2 from water via ZOWS under visible light (Figure 2b). An excess of the reducing component of the redox couple ($[Co(bpy)_3]^{2+}$) initially resulted in non-stoichiometric release rates of H_2 and O_2. However, as the reaction progressed, the H_2 to O_2 ratio gradually approached the expected stoichiometric value of 2:1, indicating that the concentrations of $[Co(bpy)_3]^{2+}$ and $[Co(bpy)_3]^{3+}$ had stabilized.[15, 20] The average H_2 and O_2 evolution rates over a 10 h time span were 3.0 and 1.5 μmol h^{-1}, respectively. After stabilisation of $[Co(bpy)_3]^{2+}$ and $[Co(bpy)_3]^{3+}$ concentrations and degassing of the system, hydrogen and oxygen were evolved in a stoichiometric ratio, with negligible performance degradation, demonstrating the robust stability of the Z-scheme system. The AQY of this redox-mediated ZOWS system was determined to be 0.1% at approximately 420 nm (Figure S6).

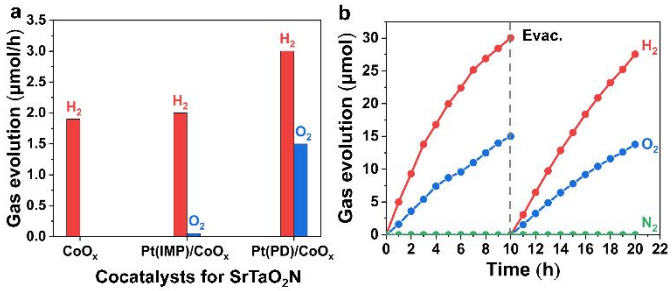

Figure 2. (a) Photocatalytic activity for ZOWS system over 10 h time span using $SrTaO_2N$ modified with various cocatalysts. (b) Gas evolution over time during ZOWS reaction under visible light. Reaction conditions: 50 mg HEP (Cr_2O_3/Pt/$BaTaO_2N$:Zr, 0.9 wt% Cr and 0.3 wt% Pt) and 100 mg OEP (Pt(PD)/CoO_x/$SrTaO_2N$, 0.2 wt% Co and 0.2 wt% Pt); 150 mL of a 25 mM sodium phosphate buffer solution (pH 8) containing 1 mM $[Co(bpy)_3]^{3+/2+}$ ions; 300 W Xe lamp ($\lambda \geq 420$ nm).

The efficacy of $SrTaO_2N$ as an OEP in the present ZOWS system was significantly enhanced by the loading of dual cocatalysts comprising Pt applied by photodeposition and CoO_x applied by impregnation. The effect of the dual cocatalyst structure on ZOWS activity was examined by assessing the morphology of the $SrTaO_2N$ with the cocatalysts using scanning transmission electron microscopy (STEM). The ADF-STEM image and energy-dispersive X-ray spectroscopy (EDS) elemental maps in Figure 3 show the distributions of the Pt and CoO_x cocatalysts. It is apparent that photodeposition preferentially loaded the Pt cocatalyst on the {100} crystal facets.[7, 27] Even so, some Pt was found in the same locations as the CoO_x, presumably due to the adsorption and reaction of H_2PtCl_6 on the CoO_x during the photodeposition process. X-ray photoelectron spectroscopy (XPS) was also employed to examine the valence states of the cocatalysts. The presence of characteristic Co and Pt peaks in the resulting spectra confirmed that both CoO_x and Pt were loaded (Figure S7). The chemical state of the Co was unchanged during the photodeposition of Pt (Figure S8), suggesting that the Pt and CoO_x cocatalysts were present on the substrate independent of one another and did not interact in a manner that affected their catalytic properties.

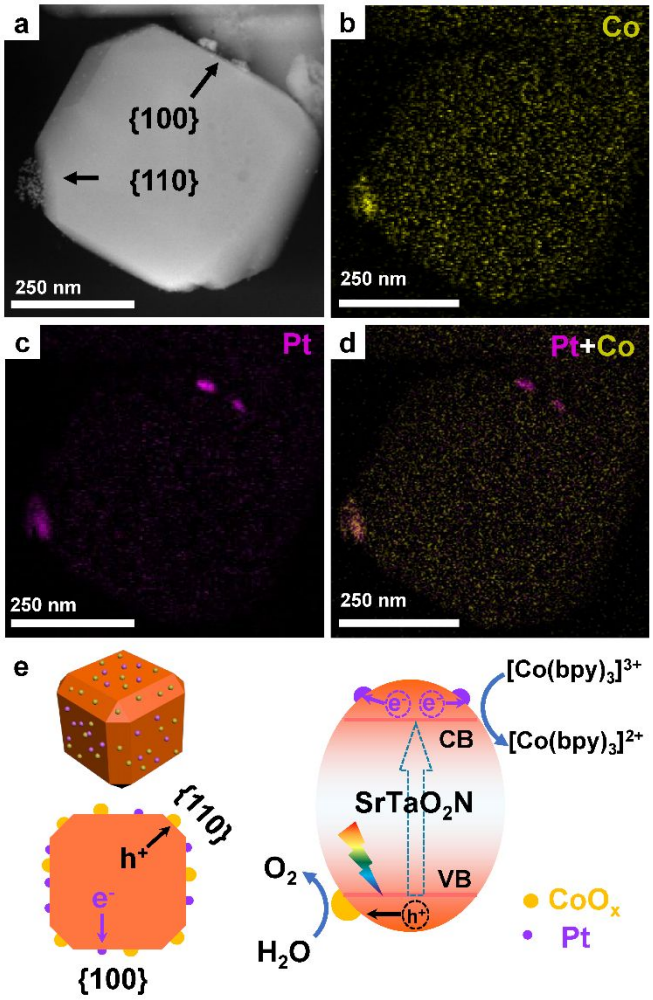

Figure 3. (a) ADF-STEM image of Pt(PD)/CoO_x/$SrTaO_2N$ and STEM-EDS elemental maps showing (b) Co, (c) Pt and (d) superimposed Pt and Co signals. (e) Diagrams showing structure and function of Pt(PD)/CoO_x/$SrTaO_2N$ when acting as OEP in ZOWS system.

It is worth noting that, although the AQY obtained from this material remained unsatisfactory, this system extended the range of visible light usable for ZOWS to nearly 600 nm based on the simultaneous utilization of oxynitrides as both the HEP and OEP. The successful function of the $SrTaO_2N$ as the OEP in the present system can be attributed to the synergistic effect of charge separation induced by the crystalline $SrTaO_2N$ particles having exposed anisotropic facets and the enhanced activity provided by the dual cocatalysts. The distinct crystalline planes of the $SrTaO_2N$ allowed spatial isolation of the Pt and CoO_x cocatalysts during the photodeposition process, although this separation was admittedly imperfect. The incorporation of the two cocatalysts also promoted reduction of the redox mediator ($[Co(bpy)_3]^{3+}$) and oxidation of water, thereby allowing the $SrTaO_2N$ to function efficiently in this ZOWS system.

The synergistic effect obtained from using the anisotropic crystalline $SrTaO_2N$ particles and the dual cocatalysts (Pt(PD) and CoO_x) was further examined by assessing the O_2 evolution performance of the $SrTaO_2N$ combined with $[Fe(CN)_6]^{3-}$ as an electron acceptor. As shown in Figure S9 in the ESI, in the absence of Pt loading or with non-selective Pt loading, the O_2 evolution activity was negligibly low. However, following Pt loading via photodeposition, a notable increase in O_2 evolution activity was achieved. Upon incorporation of $[Fe(CN)_6]^{3-/4-}$ as a redox mediator, the Z-scheme system composed of Pt(PD)/CoO_x/$SrTaO_2N$ and Cr_2O_3/Pt/$BaTaO_2N$:Zr successfully achieved water splitting under visible light, producing H_2 and O_2 in a stoichiometric ratio. This observation is consistent with earlier studies concerning the benefits of dual cocatalyst systems and highlights the importance of cocatalyst placement with regard to achieving efficient ZOWS.[7, 17]

The pH of the reaction solution often has a significant effect on the activity of a ZOWS system. Figure 4a demonstrates changes in the ZOWS activity of the $BaTaO_2N$:Zr-$[Co(bpy)_3]^{3+/2+}$-$SrTaO_2N$ system with variations in pH. In the case that the pH of the reaction solution deviated from 8, the ZOWS activity decreased significantly. In addition, although H_2 evolution was relatively constant from pH 6 to 8, the output of this product was diminished at pH 10. In contrast, the extent of O_2 evolution was negligible below pH 7. These effects of pH can be explained based on the energy diagram for the Z-scheme system provided in Figure 4b. The band structure of $SrTaO_2N$ and $BaTaO_2N$:Zr was determined by a combined analysis of Mott-Schottky (MS) measurements and Tauc plot analysis derived from DRS.[37-39] The flat band potentials for $SrTaO_2N$ and $BaTaO_2N$:Zr were estimated to be −0.35 V and −0.40 V (vs. normal hydrogen electrode (NHE), pH = 7), respectively (Figure S10a and S10b). Typically, the conduction band of n-type semiconductors lies approximately 0.1 V more negative than the flat band potential, thus the conduction band of SrTaO2N and $BaTaO_2N$ were −0.45 and −0.5 V (vs, NHE, pH = 7), respective.[40] The optical bandgaps calculated from the DRS data were 2.20 eV for $SrTaO_2N$ and 2.05 eV for $BaTaO_2N$:Zr (Figure S10c), with their respective valence band positions determined to be 1.75 and 1.55 V (vs. NHE, pH = 7). The bandgap potentials of oxynitride semiconductors and the H^+/H_2 and O_2/H_2O redox potentials are known to change with pH according to the Nernst equation, although the relative potentials remain unchanged at all pH levels. In addition, electrochemical analyses have demonstrated that the redox potential of the $[Co(bpy)_3]^{3+/2+}$ ion pair, which does not involve H^+, is unaffected by pH.[36, 41] Consequently, the bandgap potential of the $SrTaO_2N$ was shifted negatively with respect to the redox potential of $[Co(bpy)_3]^{3+/2+}$ at higher pH values (Figure S10a). This phenomenon, in turn, promoted the reduction of $[Co(bpy)_3]^{3+}$ ions by photogenerated electrons. The CoO_x used as a cocatalyst has also been found to exhibit superior water oxidation performance in alkaline environments. Linear sweep voltammetry (LSV) data acquired in this work established that Pt(PD)/CoO_x/$SrTaO_2N$ photoanodes provided higher photocurrent densities at alkaline pH values compared with neutral pH under simulated solar radiation (Figure 4c). This effect facilitated the O_2 evolution reaction and improved the ZOWS performance at pH 8. However, at pH 10, the ZOWS activity was decreased due to the dissolution of Cr_2O_3, which was essential to avoid backward reactions. Conversely, under acidic conditions, the driving force for the reduction of $[Co(bpy)_3]^{3+}$ by photogenerated electrons was lowered, thus decreasing the O_2 evolution activity. As such, the simultaneous evolution of H_2 and O_2 did not occur. Finally, the competing reaction involving the oxidation of $[Co(bpy)_3]^{2+}$ ions likely also lowered the extent of O_2 evolution on the $SrTaO_2N$.

Despite achieving ZOWS based solely on oxynitrides through dual cocatalyst loading, the loading of the Pt cocatalyst onto the $SrTaO_2N$ inevitably induced O_2 reduction, a backward reaction. As such, the Pt(PD)/CoO_x/$SrTaO_2N$/Ti photoanode generated a greater O_2 reduction current compared with the CoO_x/$SrTaO_2N$/Ti photoanode in the absence of light (Figure S11). This reverse reaction reduced the performance of the present ZOWS system relative to those of $BaTaO_2N$-$BiVO_4$ and $BaTaO_2N$-WO_3 systems using oxide OEPs reported in the literature.[19, 20]

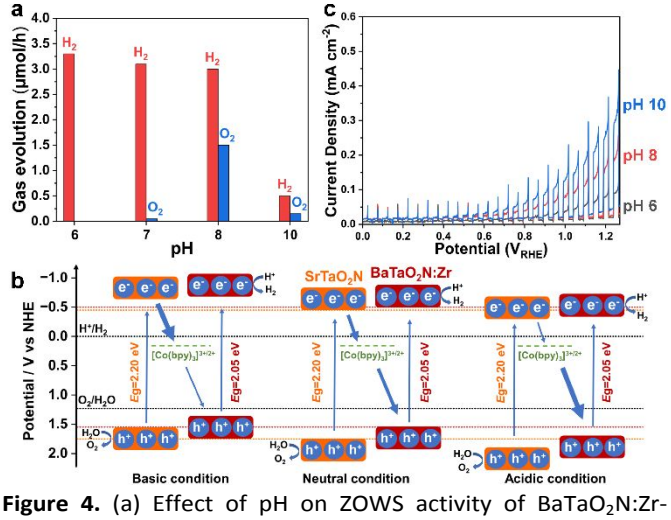

Figure 4. (a) Effect of pH on ZOWS activity of $BaTaO_2N$:Zr-$[Co(bpy)_3]^{3+/2+}$-$SrTaO_2N$ system. Reaction conditions: 50 mg HEP (Cr_2O_3/Pt/$BaTaO_2N$:Zr, 0.9 wt% Cr and 0.3 wt% Pt) and 100 mg OEP (Pt(PD)/CoO_x/$SrTaO_2N$, 0.2 wt% Co and 0.2 wt% Pt); 150 mL of a 25 mM sodium phosphate buffer solution (pH

6-10) containing 1 mM $[Co(bpy)_3]^{3+/2+}$ ions; 300 W Xe lamp ($\lambda \geq$ 420 nm). (b) Energy diagrams for Z-scheme system based on $BaTaO_2N$:Zr-$[Co(bpy)_3]^{3+/2+}$-$SrTaO_2N$ under basic, neutral and acidic conditions. (c) LSV data acquired from Pt(PD)/CoO_x/$SrTaO_2N$/Ti photoanodes under chopped irradiation with simulated sunlight in 0.1 M phosphate buffer solutions (pH 6-10).

Conclusions

A ZOWS system consisting solely of oxynitride photocatalysts capable of evolving H_2 and O_2 in a stoichiometric ratio using visible light up to nearly 600 nm was constructed using Pt(PD)/CoO_x/$SrTaO_2N$, Cr_2O_3/Pt/$BaTaO_2N$ and $[Co(bpy)_3]^{3+/2+}$ as the OEP, HEP and redox mediator, respectively. The use of Pt(PD) and CoO_x as dual cocatalysts to promote the reduction and oxidation reactions, respectively, effectively activated the $SrTaO_2N$ for both $[Co(bpy)_3]^{3+}$ reduction and water oxidation. Consequently, the material was able to function as the OEP in the ZOWS system. This study demonstrated that the fabrication of anisotropic crystal planes and the formation of highly crystalline single crystals by molten salt-assisted nitridation enabled the spatial isolation of the reduction and oxidation co-catalysts. This effect, in turn, reduced carrier recombination and provided more efficient charge separation in the $SrTaO_2N$. These results provide important insights and guidelines regarding the design and assembly of ZOWS systems driven by long-wavelength visible light for efficient solar energy conversion.

Experimental

Chemicals and materials

Ta_2O_5 was purchased from High Purity Chemicals. $BaCO_3$ and $SrCO_3$ were purchased from the Kanto Chemical Co., Inc. $ZrO(NO_3)_2{\cdot}2H_2O$, NaCl, RbCl, NaOH, $H_2PtCl_6{\cdot}6H_2O$, K_2CrO_4, $Co(NO_3)_2{\cdot}6H_2O$, Na_2HPO_4, NaH_2PO_4, $AgNO_3$, $CoSO_4{\cdot}7H_2O$, 2,2′-bipyridine and $K_3Fe(CN)_6$ were obtained from FUJIFILM Wako Pure Chemical Corp. All reagents were used directly as received without further purification.

Synthesis of HEP (Cr_2O_3/Pt/$BaTaO_2N$:Zr)

$BaTaO_2N$:Zr was synthesized via a one-step nitridation using a molten RbCl flux, following a previously reported procedure.[18, 20] $ZrO(NO_3)_2{\cdot}2H_2O$, $BaCO_3$ and Ta_2O_5 were combined to give a Ba:Ta:Zr molar ratio of 1.1:1:0.01 and then mixed with RbCl at a solute concentration of 10 mol%. This mixture was thoroughly ground for 30 min to ensure a uniform composition and then heated to 950 °C and held at that temperature for 6 h under an NH_3 flow (200 mL min^{-1}). Following nitridation, the product was washed three times with water and subsequently dried under vacuum at 40 °C for 6 h.

The cocatalysts were deposited onto the $BaTaO_2N$:Zr by impregnation followed by H_2 reduction.[19] Initially, 110 mg of $BaTaO_2N$:Zr was dispersed in an aqueous solution containing $H_2PtCl_6{\cdot}6H_2O$ and NaOH as precursors, in which the Pt and Na concentrations were 0.3 and 0.23 wt%, respectively, relative to the photocatalyst mass. The resulting dispersion was subsequently heated on a boiling water bath until it was completely dry. The remaining powder was recovered and subsequently heated at 350 °C for 1 h in a flow of 10% H_2 in N_2. The resulting Pt/$BaTaO_2N$:Zr was additionally modified with Cr_2O_3 by photodeposition to suppress competing reactions. This was accomplished by dispersing a quantity of the Pt/$BaTaO_2N$:Zr powder in 150 mL of an aqueous methanol solution (15 vol%), after which K_2CrO_4 was added as a Cr^{6+} precursor without pH adjustment. The amount of Cr_2O_3 added was nominally equivalent to a loading of 0.9 wt% Cr with respect to the photocatalyst mass. After degassing, the suspension was irradiated with visible light ($\lambda \geq$ 420 nm) for 1 h. The photocatalyst was then removed by filtration, washed with ultrapure water, and dried at 40 °C under vacuum.

Synthesis of OEP (Pt(PD)/CoO_x/$SrTaO_2N$)

Single crystalline $SrTaO_2N$ particles were fabricated through the nitridation of a blend of Ta_2O_5, $SrCO_3$ and NaCl (combined in a molar ratio of 0.5:1.1:9) under an NH_3 flow.[32] In a representative synthesis, 0.357 g of Ta_2O_5, 0.486 g of $SrCO_3$ and 1.157 g of NaCl were mixed for 30 min. The blended mixture was then transferred to an alumina crucible and heated at 950 °C for 6 h under an NH_3 flow at a rate of 100 mL min^{-1}. After the nitridation process, the synthesized product was washed three times with water, followed by drying under vacuum at 40 °C for 6 h. As a control experiment, a sample was also synthesized via the direct nitridation of a mixture of Ta_2O_5 and $SrCO_3$ having a molar ratio of 0.5:1.1, using the SSR method. This material is referred to herein as the $SrTaO_2N$(SSR).

The preparation of the cocatalyst-loaded $SrTaO_2N$ involved a sequential two-step process, starting with the loading of CoO_x through impregnation and nitridation, followed by the additional loading of Pt via photodeposition. The resulting sample is denoted herein as Pt(PD)/CoO_x/$SrTaO_2N$, where PD indicates photodeposition. The $SrTaO_2N$ powder was initially immersed in an aqueous solution containing an appropriate amount of $Co(NO_3)_2{\cdot}6H_2O$ serving as the Co precursor. This mixture was homogenized using a combination of sonication and stirring after which the water was evaporated by heating over a hot water bath. The dried sample was subsequently calcined at 950 °C for 1 h under a 200 mL min^{-1} flow of gaseous NH_3 to produce the CoO_x/$SrTaO_2N$ photocatalyst. This product was then dispersed in 150 mL of a 15 vol% aqueous methanol solution, to which a specific quantity of $H_2PtCl_6{\cdot}6H_2O$, acting as the Pt precursor, was added. Following degassing, the suspension was exposed to visible light ($\lambda \geq$ 420 nm) for 4 h. Finally, the photocatalyst was recovered by filtration, rinsed with ultrapure water and vacuum-dried at 40 °C. For comparison purposes, Pt was also loaded via impregnation followed by reduction under hydrogen. Briefly, a suitable amount of the CoO_x/$SrTaO_2N$ sample was immersed in an aqueous solution of $H_2PtCl_6{\cdot}6H_2O$ such that the Pt

concentration relative to the photocatalyst mass was 0.2 wt%. The mixture was then subjected to ultrasonic stirring for approximately one minute. Following this, the water was completely evaporated using a water bath, after which the impregnated powder was collected and then reduced by heating at 200 °C for 1 h under a flow of 10% H_2 in N_2 (200 mL min^{-1}). The resulting powder is denoted herein as Pt(IMP)/CoO_x/$SrTaO_2N$, where IMP indicates impregnation

Preparation of the $[Co(bpy)_3]SO_4$

$[Co(bpy)_3]SO_4$ was synthesized following a method previously described in the literature.[36] Briefly, a 3 M aqueous $CoSO_4$ solution was slowly added to a 2 M 2,2'-bipyridine solution in ethanol. The resulting precipitate was isolated through suction filtration and then washed with a 9:1 mixture of acetone and water.

Characterization

The crystal phases of the various products were assessed by XRD using a Rigaku MiniFlex 300 powder diffractometer with a Cu Kα radiation source (λ = 1.5418 Å). DRS data were acquired using an ultraviolet-visible-near-infrared spectrometer (V-670, JASCO) with conversion of the data from reflectance to the Kubelka-Munk function. The valence states of the metals in the Pt(PD)/CoO_x/$SrTaO_2N$ were examined using XPS (PHI Quantera II, ULVAC-PHI, Inc.) with an Al Kα radiation source. The morphologies and structures of the materials produced in this work were investigated by field-emission SEM (Hitachi, SU8000). High-resolution TEM images together with EDS elemental maps were also acquired, using a JEOL JEM-2800 instrument.

Photocatalytic O_2 evolution and ZOWS reactions

All photocatalytic reactions were conducted using a Pyrex top-illuminated reaction vessel held at 17 °C and connected to a closed gas circulation system. Temperature control was achieved through a cooling water system. In the case of the O_2 evolution reaction, Pt(PD)/CoO_x/$SrTaO_2N$ (100 mg) was dispersed in 150 mL of a 25 mM sodium phosphate buffer solution (pH 8) containing 5 mM $K_3[Fe(CN)_6]$. Cr_2O_3/Pt/$BaTaO_2N$:Zr (50 mg) serving as the HEP and Pt(PD)/CoO_x/$SrTaO_2N$ (100 mg) acting as the OEP were dispersed in 150 mL of a 25 mM sodium phosphate buffer solution (pH 8) containing 1 mM $[Co(bpy)_3]^{3+/2+}$ ions for the photocatalytic ZOWS reaction. After completely degassing the photocatalyst suspension by evacuation, Ar gas was introduced to generate a background pressure of approximately 10 kPa. The reactant solution was then irradiated with a 300 W Xe lamp equipped with a dichroic mirror and a cut-off filter (L42, $\lambda \geq 420$ nm). The gaseous products generated by the solution were analysed using a gas chromatography system integrated into the closed circulation system. This instrumentation consisted of a gas chromatograph (Shimadzu, GC-2014) equipped with molecular sieve 5 Å columns and a thermal conductivity detector, employing Ar as the carrier gas.

Apparent quantum yield assessments

The AQY for each ZOWS system was determined under the same experimental conditions described above except for the use of a 300 W Xe lamp (MAX-303 Compact Xenon Light Source, Asahi Spectra) equipped with bandpass filters having central wavelengths of 420, 460, 500, 540, 600 or 640 nm (full width at half-maximum = 10 nm). The number of incident photons was measured using an LS-100 grating spectroradiometer (EKO Instruments Co., Ltd.). The AQY was calculated according to the equation[42, 43]

$$\mathrm{AQY}(\%) = \frac{[4 \times n(\mathrm{H_2})]}{n(\mathrm{photons})} \times 100$$

where $n(H_2)$ and n(photons) are the quantities of evolved H_2 molecules and incident photons, respectively.

Photoelectrochemical measurements

Each $SrTaO_2N$ photoanode was fabricated using the particle transfer technique. Briefly, 10 mg of the Pt(PD)/CoO_x/$SrTaO_2N$ dispersed in isopropyl alcohol was drop-cast onto a 3 cm × 1 cm glass substrate. Following drying, a Ti layer was deposited on the sample surface using radio-frequency magnetron sputtering. Subsequently, the Ti/photocatalyst layer composite was peeled off, affixed to another glass plate, and subjected to sonication to eliminate excess particles loosely attached to the particle layer. Finally, an electric wire was connected using indium solder. The photoelectrochemical properties of the photoanodes were assessed in a three-electrode setup, employing a Pt wire as the counter electrode and an Ag/AgCl electrode in a saturated KCl solution as the reference electrode. The experiments utilized a potentiostat (HSV-100, Hokuto Denko) with electrode potentials converted to reversible H_2 electrode (RHE) values using the Nernst equation. A 0.1 M phosphate buffer solution adjusted to a pH value in the range of 6-10 served as the electrolyte, with Ar gas purging and continuous magnetic stirring. LSV measurements, conducted from positive to negative potentials at a scan rate of 10 mV s^{-1}, were performed under chopped illumination from a solar simulator (XES-40S1, SAN-EI ELECTRIC). The flat band potentials of the photoelectrodes were determined through MS analysis, with plots recorded in the dark over a potential range of −0.4 V to 0.6 V (vs. NHE) at a fixed frequency of 1000 Hz.

Author contributions

T.H. and K.D. designed and supervised the research. W.L., A.H. and R.A.G. carried out the experiments. M.N. carried out the STEM–EDS analyses and evaluated the resulting data. S.S. and F.W. conducted the photoelectrochemical experiments and analysed the resulting data. W.L., A.H., R.A.G., F.W., S.S., T.H. and K.D. discussed the results. W.L., T.H. and K.D. wrote the manuscript with contributions from the other authors.

Conflicts of interest

The authors declare no competing financial interests.

Data availability

The data supporting this article have been included as part of the ESI. Data are also available upon request from the authors.

Acknowledgements

This research was supported by JST, PRESTO, Japan (grant no. JPMJPR20T9), the Artificial Photosynthesis Project (ARPChem) of the New Energy and Industrial Technology Development Organization (NEDO), Advanced Research Infrastructure for Materials and Nano-technology in Japan (ARIM) of the Ministry of Education, Culture, Sports, Science and Technology (MEXT) (grant no. JPMXP1224UT0040) and the China Scholarship Council (grant no. 202008440289). W.L. also acknowledges the financial support of a 2021 MEXT Scholarship with Embassy Recommendation. The authors thank Ms. Michiko Obata of Shinshu University for assistance during the XPS analyses.

Notes and references

1. T. Hisatomi, J. Kubota and K. Domen, *Chem. Soc. Rev.*, 2014, **43**, 7520-7535.
2. Y. Wang, H. Suzuki, J. Xie, O. Tomita, D. J. Martin, M. Higashi, D. Kong, R. Abe and J. Tang, *Chem. Rev.*, 2018, **118**, 5201-5241.
3. Q. Wang and K. Domen, *Chem. Rev.*, 2020, **120**, 919-985.
4. D. Zhao, Y. Wang, C.-L. Dong, Y.-C. Huang, J. Chen, F. Xue, S. Shen and L. Guo, *Nat. Energy*, 2021, **6**, 388-397.
5. Y. Fang, Y. Hou, X. Fu and X. Wang, *Chem. Rev.*, 2022, **122**, 4204-4256.
6. T. Hisatomi and K. Domen, *Nat. Catal.*, 2019, **2**, 387-399.
7. Y. Qi, Y. Zhao, Y. Gao, D. Li, Z. Li, F. Zhang and C. Li, *Joule*, 2018, **2**, 2393-2402.
8. J. Xiao, M. Nakabayashi, T. Hisatomi, J. J. M. Vequizo, W. Li, K. Chen, X. Tao, A. Yamakata, N. Shibata, T. Takata, Y. Inoue and K. Domen, *Nat. Commun.*, 2023, **14**, 8030.
9. L. Lin, Y. Ma, J. J. M. Vequizo, M. Nakabayashi, C. Gu, X. Tao, H. Yoshida, Y. Pihosh, Y. Nishina, A. Yamakata, N. Shibata, T. Hisatomi, T. Takata and K. Domen, *Nat. Commun.*, 2024, **15**, 397.
10. L. Lin, Y. Ma, N. Zettsu, J. J. M. Vequizo, C. Gu, A. Yamakata, T. Hisatomi, T. Takata and K. Domen, *J. Am. Chem. Soc.*, 2024, **146**, 14829-14834.
11. L. Lin, Z. Lin, J. Zhang, X. Cai, W. Lin, Z. Yu and X. Wang, *Nat. Catal.*, 2020, **3**, 649-655.
12. S. Navalón, A. Dhakshinamoorthy, M. Álvaro, B. Ferrer and H. García, *Chem. Rev.*, 2023, **123**, 445-490.
13. N. Iwasa, H. Sandaiji, S. Nandy, M. Nakabayashi, T. Takata, T. Hisatomi and K. Domen, *J. Mater. Chem. A*, 2024, **12**, 20247-20255.
14. G. Wan, L. Yin, X. Chen, X. Xu, J. Huang, C. Zhen, H. Zhu, B. Huang, W. Hu, Z. Ren, H. Tian, L. Wang, G. Liu and H.-M. Cheng, *J. Am. Chem. Soc.*, 2022, **144**, 20342-20350.
15. K. Maeda, D. Lu and K. Domen, *ACS Catal.*, 2013, **3**, 1026-1033.
16. K. Chen, J. Xiao, J. J. M. Vequizo, T. Hisatomi, Y. Ma, M. Nakabayashi, T. Takata, A. Yamakata, N. Shibata and K. Domen, *J. Am. Chem. Soc.*, 2023, **145**, 3839-3843.
17. Y. Qi, J. Zhang, Y. Kong, Y. Zhao, S. Chen, D. Li, W. Liu, Y. Chen, T. Xie, J. Cui, C. Li, K. Domen and F. Zhang, *Nat. Commun.*, 2022, **13**, 484.
18. H. Li, J. J. M. Vequizo, T. Hisatomi, M. Nakabayashi, J. Xiao, X. Tao, Z. Pan, W. Li, S. Chen, Z. Wang, N. Shibata, A. Yamakata, T. Takata and K. Domen, *EES Catal.*, 2023, **1**, 26-35.
19. H. H. Li, D. L. Lu, S. S. Chen, T. Hisatomi, J. J. M. Vequizo, J. D. Xiao, Z. Wang, L. H. Lin, Q. Xiao, Y. L. Sun, Y. Miseki, K. Sayama, A. Yamakata, T. Takata and K. Domen, *J. Mater. Chem. A*, 2021, **9**, 13851-13854.
20. W. Li, H. Li, Y. Ma, J. Xiao, D. Lu, T. Hisatomi and K. Domen, *J. Catal.*, 2023, **428**, 115187.
21. Y. Qi, B. Zhang, G. Zhang, Z. Zheng, T. Xie, S. Chen, G. Ma, C. Li, K. Domen and F. Zhang, *Joule*, 2024, **8**, 193-203.
22. M. Thangamuthu, K. Vankayala, L. Xiong, S. Conroy, X. Zhang and J. Tang, *ACS Catal.*, 2023, **13**, 9113-9124.
23. J. Fu and S. E. Skrabalak, *Angew. Chem. Int. Ed.*, 2017, **56**, 14169-14173.
24. X. Sun, F. Wu, G. Liu and X. Xu, *J. Mater. Chem. A*, 2018, **6**, 20760-20768.
25. M. M. Kodera, Yugo Sayama, Kazuhiro, *ACS Appl. Energy Mater.*, 2024, **7**, 675-680.
26. H. A. Kumagai, Ryosuke Kato, Kosaku Yamakata, Akira Kakihana, Masato Kato, Hideki, *ACS Appl. Energy Mater.*, 2021, **4**, 2056-2060.
27. T. Takata, J. Jiang, Y. Sakata, M. Nakabayashi, N. Shibata, V. Nandal, K. Seki, T. Hisatomi and K. Domen, *Nature*, 2020, **581**, 411-414.
28. J. Pan, G. Liu, G. Q. Lu and H.-M. Cheng, *Angew. Chem. Int. Ed.*, 2011, **50**, 2133-2137.
29. R. Chen, Z. Ren, Y. Liang, G. Zhang, T. Dittrich, R. Liu, Y. Liu, Y. Zhao, S. Pang, H. An, C. Ni, P. Zhou, K. Han, F. Fan and C. Li, *Nature*, 2022, **610**, 296-301.
30. T. Suguro, F. Kishimoto, N. Kariya, T. Fukui, M. Nakabayashi, N. Shibata, T. Takata, K. Domen and K. Takanabe, *Nat. Commun.*, 2022, **13**, 5698.
31. Z. Wang, Y. Luo, T. Hisatomi, J. J. M. Vequizo, S. Suzuki, S. Chen, M. Nakabayashi, L. Lin, Z. Pan, N. Kariya, A. Yamakata, N. Shibata, T. Takata, K. Teshima and K. Domen, *Nat. Commun.*, 2021, **12**, 1005.
32. R. A. Galvao, S. Nandy, A. Hirako, T. Otsuki, M. Nakabayashi, D. Lu, T. Hisatomi and K. Domen, *Small*, 2024, **20**, e2311170.
33. Z. Yuan, C. Liu, S. Chen and F. Zhang, *J. Mater. Chem. A*, 2024, **12**, 5040-5054.
34. K. Obata, T. Higashi, F. Ye, M. Katayama and K. Takanabe, *ChemPhotoChem*, 2023, **7**, e202200293.
35. Y. Luo, S. Suzuki, Z. Wang, K. Yubuta, J. J. M. Vequizo, A. Yamakata, H. Shiiba, T. Hisatomi, K. Domen and K. Teshima, *ACS Appl. Mater. Interfaces*, 2019, **11**, 22264-22271.
36. Y. Sasaki, H. Kato and A. Kudo, *J. Am. Chem. Soc.*, 2013, **135**, 5441-5449.
37. S. Li, H. Shang, Y. Tao, P. Li, H. Pan, Q. Wang, S. Zhang, H. Jia, H. Zhang, J. Cao, B. Zhang, R. Zhang, G. Li, Y. Zhang, D. Zhang and H. Li, *Angew. Chem. Int. Ed.*, 2023, **62**, e202305538.
38. P. Dong, X. Xu, R. Luo, S. Yuan, J. Zhou and J. Lei, *J. Am. Chem. Soc.*, 2023, **145**, 15473-15481.
39. B. Su, Y. Kong, S. Wang, S. Zuo, W. Lin, Y. Fang, Y. Hou, G. Zhang, H. Zhang and X. Wang, *J. Am. Chem. Soc.*, 2023, **145**, 27415-27423.

40. B.-B. Luan, X. Chu, Y. Wang, X. Qiao, Y. Jiang and F.-M. Zhang, *Adv. Mater.*, 2024, **36**, 2412653.
41. D. Dung, J. Ramsden and M. Graetzel, *J. Am. Chem. Soc.*, 1982, **104**, 2977-2985.
42. T. Hisatomi and K. Domen, *Nature Sustainability*, 2024, **7**, 1082-1084.
43. Z. L. Wang, T. Hisatomi, R. G. Li, K. Sayama, G. Liu, K. Domen, C. Li and L. Z. Wang, *Joule*, 2021, **5**, 344-359.

The data supporting this article have been included as part of the ESI. Data are also available upon request from the authors.